Radiation Physics and Chemistry 223 (2024) 111965

Contents lists available at ScienceDirect

Radiation Physics and Chemistry

journal homepage: www.elsevier.com/locate/radphyschem

Step-by-step of 3D printing a head-and-neck phantom: Proposal of a methodology using fused filament fabrication (FFF) technology

M. Savi [a,b], D. Villani [b,c,*], B. Andrade [a], F.A.P. Soares [a], O. Rodrigues Jr. [b], L.L. Campos [b], M.P.A. Potiens [b]

[a] Instituto Federal de Educação, Ciência e Tecnologia de Santa Catarina – IFSC, Mauro Ramos Avenue 950, Florianópolis, Brazil
[b] Instituto de Pesquisas Energéticas e Nucleares – IPEN/USP. Prof. Lineu Prestes Avenue 2242, São Paulo, Brazil
[c] Photo Injector Test Facility – PITZ, Deutsches Elektronen-Synchrotron DESY. Platanenallee 6, 15738, Zeuthen, Germany

ARTICLE INFO

Handling Editor: Dr. Chris Chantler

Keywords:
3D printing
FFF
Head-and-neck
Phantom

ABSTRACT

3D printing has evolved and become popular very quickly over the last 10 years, including its use in health and biomedical applications. Phantoms that mimic the interaction of radiation within the human body have been manufactured for many years using various technologies with great demand. However, their availability is restricted, and their cost is considerably high, especially considering exchange rates and importation taxes to Brazil. Thus, this paper aims to share the step-by-step process of 3D printing a head-and-neck phantom using fused filament fabrication (FFF) technology. A CIRS 711 Atom Max phantom CT image was used as the basis for the segmentation of the phantom. Radiopaque FFF filaments XCT-0, XCT-A, and XCT-C were used to build soft tissue, bone, and dental enamel, respectively. The phantom's design and segmentation were performed using the "3D Slicer Software," resulting in 58 different 3D models. The models were organized as 20 mm individual slabs, which were later sliced using Simplify3D software to be printed on a GTMaX Pro Core H4 3D printer coupled with a Mosaic Pallet 2S multi-material system. An imaging analysis was then performed to compare the original CIRS 711 Atom Max and the 3D printed phantom composed of 14 slabs. The proposed methodology of this study shows the possible use of tomographic images of any objects or anatomy to perform 3D prototyping of patient-specific and customized phantoms. The phantom imaging comparison shows great results using the proposed FFF filaments to mimic the main human tissues of the head-and-neck region. This methodology represents a feasible alternative to develop CT tissue-equivalent phantoms with desirable characteristics for radiation technology and biomedical applications, e.g. patient positioning, imaging techniques optimization and *in vivo* dosimetry. Additionally, the developed phantom is cost-effective and can be obtained for around 10% of the cost of a commercially available phantom in Brazil.

1. Background

Additive manufacturing (AM), commonly known as 3D Printing (3DP), is transforming the means of production of many objects and anthropomorphic phantoms can be included in the list of objects that this technology can produce. In medical physics and biomedical engineering, the 3DP is focused on creating phantoms that interact as close as possible as the human tissues while also trying to represent a specific organ or geometry of interest (ICRU, 1989; DeWerd, 2014). Many authors are conducting research worldwide to achieve the best technique to obtain the most realistic phantom, regarding anatomy and interaction with radiation (Bandyopadhyay et al., 2015; Hamedani et al., 2018; Filippou and Tsoumpas, 2018; Diamantopoulos et al., 2018; Santos et al., 2019; Villani, 2021; Pereira et al., 2021, 2022). Over the last ten years the number of publications regarding the subject rose year after year (Fig. 1).

Polyjet, Stereolithography (SLA) and Fused Filament Fabrication (FFF) are the three 3DP methods generally used to construct phantoms. PolyJet is the trademarked name for a particular type of material jetting by US-Isreali-based company Stratasys (*www.stratasys.com*). The printer deposits tiny droplets of resin that solidify almost instantly under UV light so that parts are produced layer by layer. Although not technically a distinct category of 3D printing, PolyJet has several unique features that set it apart from other processes, such as full color, rugged industrial

* Corresponding author.
E-mail address: dvillani@ipen.br (D. Villani).

https://doi.org/10.1016/j.radphyschem.2024.111965
Received 29 February 2024; Received in revised form 14 June 2024; Accepted 20 June 2024
Available online 20 June 2024

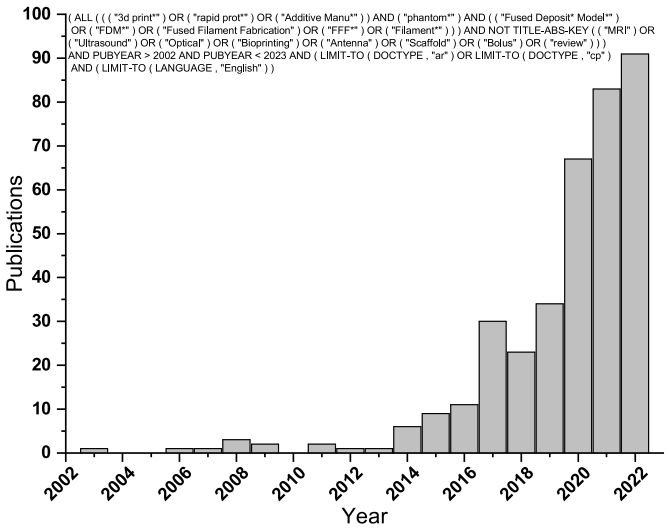

Fig. 1. Bibliometrics. Number of publications regarding 3D printing phantoms from 2002 to 2022. The syntax used in searching for articles in databases is detailed inside the figure.

parts and biocompatible dental products (Gibson et al., 2015; AII3DP, 2023). Stereolithography (SLA) is an additive manufacturing process that belongs to the vat photopolymerization family. It uses UV lasers as a light source to selectively cure a photosensitive polymer resin, layer by layer (Gibson et al., 2015). Fused Filament Fabrication (FFF) deposits melted material from a given filament layer by layer. The deposition is carried out in a specific manner dictated by a slicing software (Gibson et al., 2015).

It is already known that 3D printing patient phantoms has several pros and cons. The pros include: the technique enables patient-specific models based on individual imaging data, tailored designs for specific clinical or research needs, lower production costs compared to traditional methods, ability to simulate complex clinical scenarios. The cons rely on material limitations, as it is had to find materials mimicking human tissue properties; limited printing resolution might affect fine details within the phantom and lack of standardization and complex regulatory compliance (Rengier et al., 2010; Craft et al., 2018).

The technology chosen to pursue in our attempt to develop a 3D printed phantom is FFF, as it is the most common, widely commercially available and the cheapest 3D printing fabrication method in Brazil. In the literature three different ways to construct phantoms using FFF are reported. The first documented and widespread method is denominated '*Variable Infill Density* – VID', which consists in changing printing parameter '*infill percentage*' in the slicer program to promote material density variation and, by consequence, different interaction of radiation within the structure. This relation presents a linear trend when the interaction is measured by Hounsfield Units (HU) in Computed Tomography (CT), as determined in previous studies (Savi et al., 2020). The second way to construct phantoms with FFF is denominated '*Pixel by Pixel*' created by Okkalidis et al. (2018) and improved by Saphira et al. (2022) and then called '*Pixel Print*', which uses proprietary software to scan DICOM's pixel by pixel and transform each HU data in a specific flow of material deposited after calibration of the system.

A third method is also known and used by many authors to grant different attenuations in the same printing slice, which implies the use of more than one material. Print two or more materials can be done in three different ways, in accordance with which type of 3D printer is used. FFF printers with more than one extrusion head, like Raise 3D Pro 2 (*https://www.raise3d.com*) used by Villani et al. (2020, 2021), or Ultimaker (*https://ultimaker.com*) used by Tino et al. (2021), or even 4 heads such as Abdel Magid et al. (2018), are the first call. Alternatively, 3D printers with one head and built in filament changer, such as Bambu lab (*https://bambulab.com*), or third-party filament tool changer such as Mosaic Pallet 2S (*https://www.mosaicmfg.com*) can be used.

Comparing works and their results in literature (Hong et al., 2020; Niebuhr et al., 2019; Tong et al., 2019), pixel print produces more accurate HU variation and images visually closer to human body appearance at spences of more 3D printing time and material usage. This occurs because every pixel is printed and by consequence 100% of the slice needs to be printed, which does not occur in the other method as the variation of infill is equal for each model printed.

This paper presents the sequence of a research that has been developed throughout the past few years. From 2020 our group published studies on infill patterns and infill densities variation for 17 different materials and their radiation attenuation behavior using PMMA as reference (Savi et al., 2020, 2021; Villani et al., 2020; Oliveira et al., 2022). At that time, two main issues were found: the low infill density appears as a grid in the Computed Tomography (CT) image and there was no suitable 3D printing filament to reproduce the correct radiopacity of high attenuation tissues like cortical bone, dentin and enamel. To solve them, it was investigated the minimal infill density necessary to a CT visual homogeneity (Andrade et al., 2020a; Andrade et al., 2020b) and a new series of FFF filaments was also developed, and it is patent pending (Savi et al., 2022).

Thus, our aim with this paper is to document the step-by-step process of 3D printing a head-and-neck phantom, proposing a methodology using fused filament fabrication (FFF) 3D printing technology. The main purpose of this presented phantom is to present a cost-effective alternative to the commercial CIRS 711 Atom Max phantom in terms of Hounsfield Units and anatomy when analyzing its Computed Tomography (CT) images.

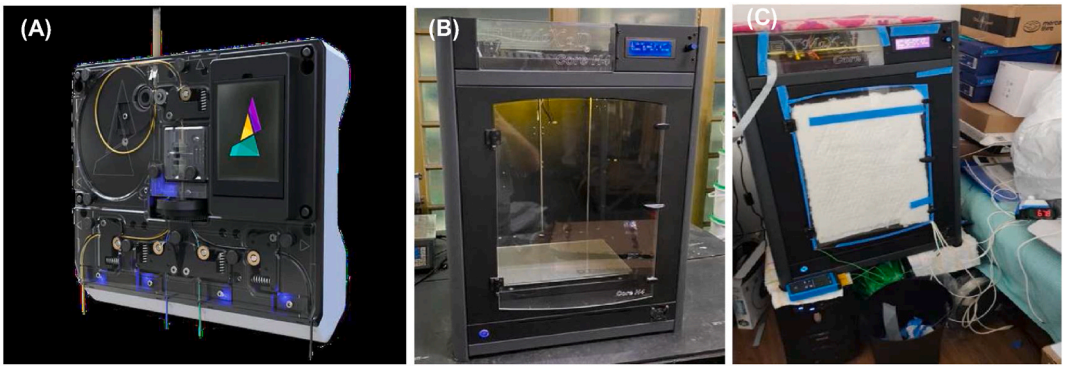

Fig. 2. The printer and the Mosaic Pallet 2S and the set-up of the 3D printing of the phantom.

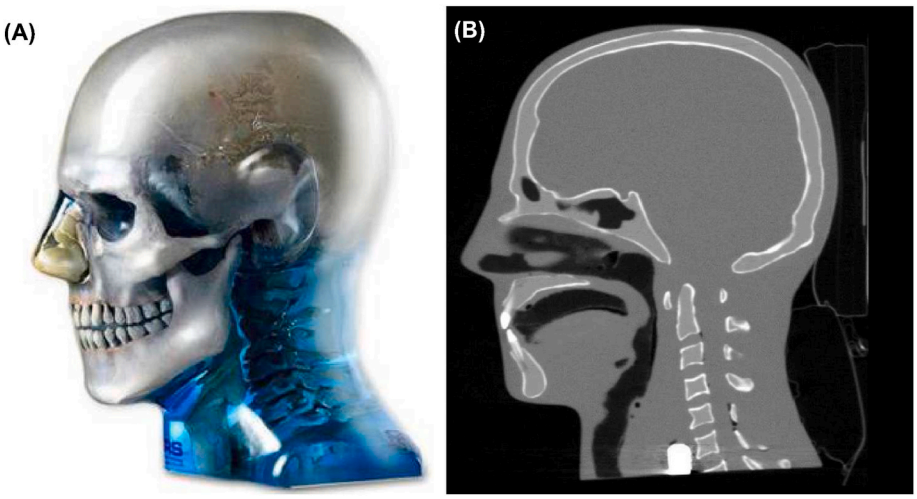

Fig. 3. CIRS ATOM 711 Anthropomorphic phantom. (A) Overview picture (B) CT image.

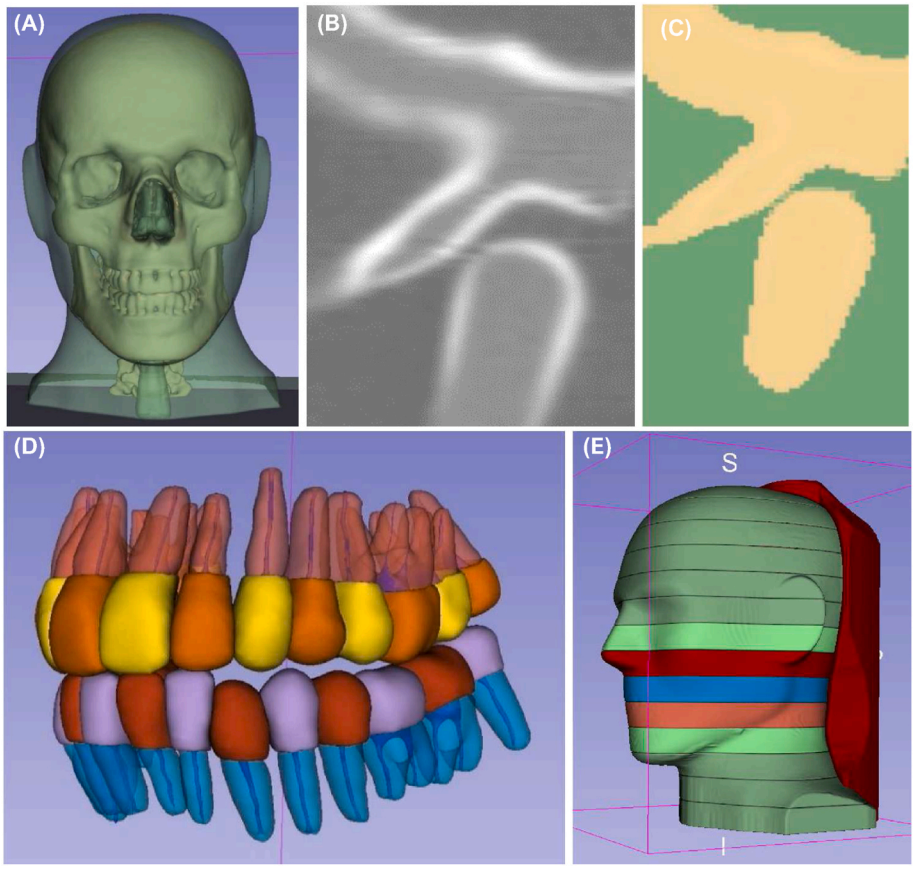

Fig. 4. Segmentation of the phantom CIRS 711. (A) Overview of the head-and-neck digital model (B) Detail of bone structure to be contoured (C) Detail on contouring of the bone structure (D) Detailed overview of the digital model of the teeth structures (E) Segmentation of the phantom into slabs.

2. Step-by-step of 3D printing a head-and-neck phantom

2.1. Reference anatomy

The CIRS 711 Atom Max (CIRS Inc., *https://www.cirsinc.com*) head-and-neck phantom was chosen to be the anatomy of reference as it avoids ethics problems from a patient CT, it is a standard in anatomy and radiation interaction in agreement with international formalisms to further comparison with the results. The presented methodology can be applied basically with any CT image of choice.

2.2. Setting up printing hardware and software

The DICOM from the CT scan of the commercial phantom was first imported in '3D Slicer' segmentation software (*https://www.slicer.org*). Then the anatomy was segmented (see section 2.3) and each originated . STL file from a slice had their own process with specific *infill* density treated in 'Simplify 3D' slicer software (see section 2.4). The .gcode was

Fig. 5. CT image of discs of different XCT filament diameters and infill percentages.

loaded in *'Chroma 3 Slicer'* software (*https://www.mosaicmfg.com/blogs/news/introducing-chroma-3*) to plan multi material 3D printing using Mosaic Pallet 2S coupled in a single extrusion GTMax 3D Core H4 printer (*https://www.gtmax3d.com.br*) (Fig. 2A and B).

The printing process of this work was performed in the south region of Brazil and we faced some problems on maintaining good room temperature during winter. Some warping problems during printing occurred, as every slab printed had 20 mm thickness of almost solid infill, besides the used material, ABS, is known to have warping problems (Ramian et al., 2021). This led to the need to internally coat the printer with ceramic wool and, as it was not sufficient, an internal heat chamber was made with an electronic thermostat (Fig. 2C).

2.3. Digital 3D model acquirement

The CIRS 711 ATOM Max phantom was used to base the shape, tissue disposition and expected attenuation. It was provided by the Federal Institute of Santa Catarina and is composed of an anatomical representation of a human head and shoulder region, resulting in a complex structure formed by different materials. Aiming to create a digital representation of the CIRS 711, the phantom was scanned in a Brilliance 64 CT (Koninklijke Philips N.V.), with parameters of 120 kVp, 0.8 mm slice thickness with 0.4 mm spacing, 26 cm FOV and standard reconstruction algorithm (later reformatted using bone reconstruction to enhance bone border profile) (Fig. 3).

The resultant DICOM images were imported to the '*3D Slicer Software*' to digitally segment the volume in different anatomies. This process involves discriminating different tissues based on its attenuation coefficient, by analyzing individual voxels Hounsfield Units values and the countering of the structures is similar with some radiation treatment planning software.

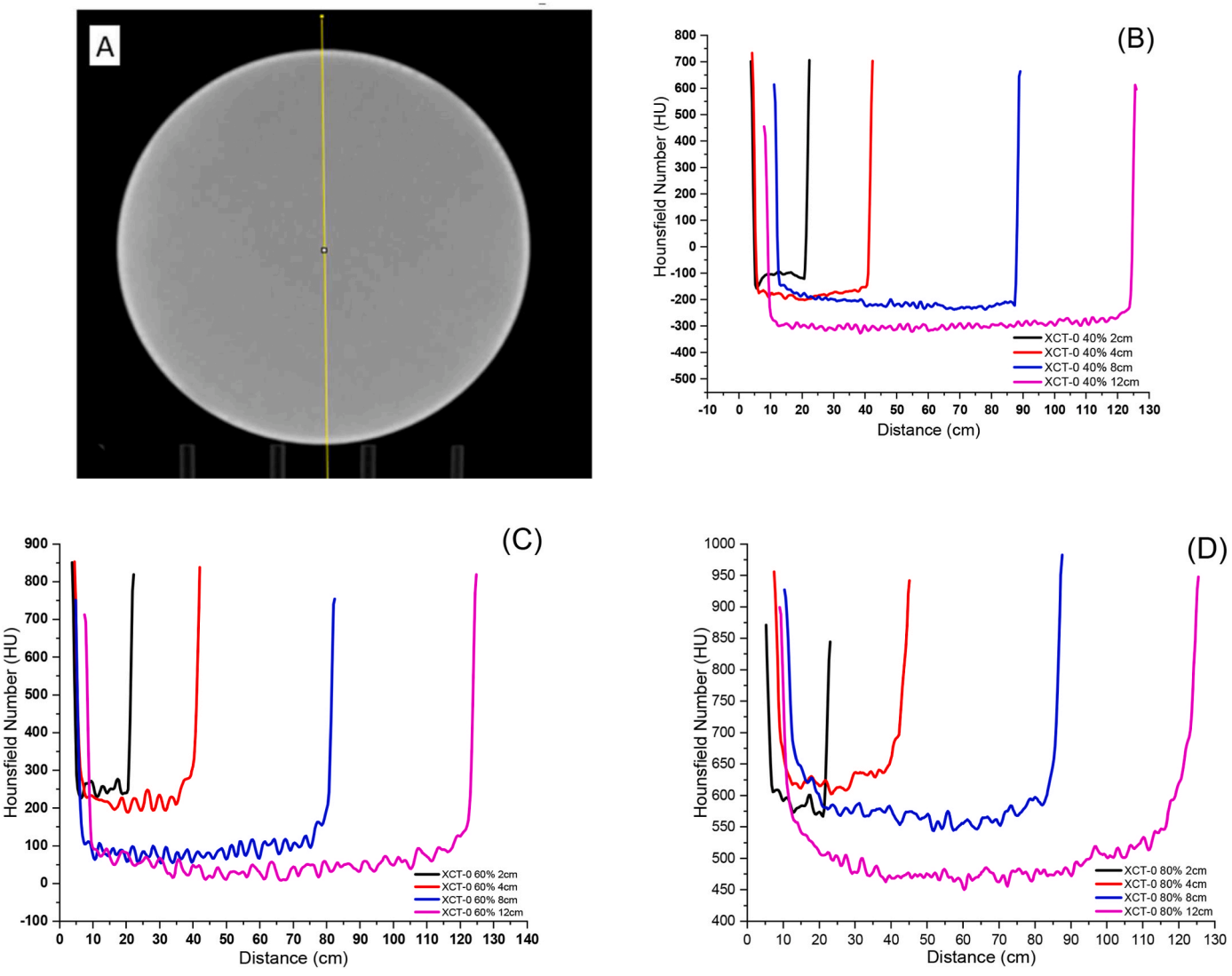

Fig. 6. (A) Linear ROI analysis on a 3D-printed XCT-0 disk; (B) (C) and (D) are the results of every disc imaged.

Table 1
Map of printing configurations according to diameter and tissues of the slab.

Model Slab	Tissue	Infill (%)	XCT	Model Slab	Tissue	Infill (%)	XCT	Model Slab	Tissue	Infill (%)	XCT
1.1	Soft	67	0	9.1	Soft	66	0	10.7	Enamel	100	C
1.2	Bone	60	A	9.2	Bone	61	A	10.8	Enamel	100	C
2.1	Soft	67	0	9.2	Jaw Bone	50	A	10.9	Enamel	100	C
2.2	Bone	60	A	9.3	Jaw Canal	–	–	10.10	Dentin	72	C
3.1	Soft	68	0	9.4	Dentin	72	C	10.11	Air	–	–
3.2	Bone	62	A	9.5	Pulp	–	–	11.1	Soft	65	0
4.1	Soft	70	0	9.6	Enamel	100	C	11.2	Bone	63	A
4.2	Bone	64	A	9.7	Enamel	100	C	11.3	Mandibular Bone	60	A
5.1	Soft	69	0	9.8	Enamel	100	C	11.4	Enamel	60	C
5.2	Bone	61	A	9.9	Enamel	100	C	12.1	Soft	64	0
6.1	Soft	66	0	9.10	Dentin	100	C	12.2	Bone	60	A
6.2	Bone	75	A	9.11	Air	–	–	13.1	Soft	64	0
7.1	Soft	66	0	10.1	Soft	65	0	13.2	Bone	60	A
7.2	Bone	71	A	10.2	Bone	58	A	14.1	Soft	64	0
8.1	Soft	66	0	10.2	Jaw Bone	60	A	14.2	Bone	63	A
8.2	Bone	64	A	10.3	Canal mandibular	–	–				
8.2	Jaw Bone	64	A	10.4	Dentin	72	C				
8.3	Jaw Canal	–	–	10.5	Pulp	–	–				
8.4	Dentine	72	C	10.6	Enamel	100	C				

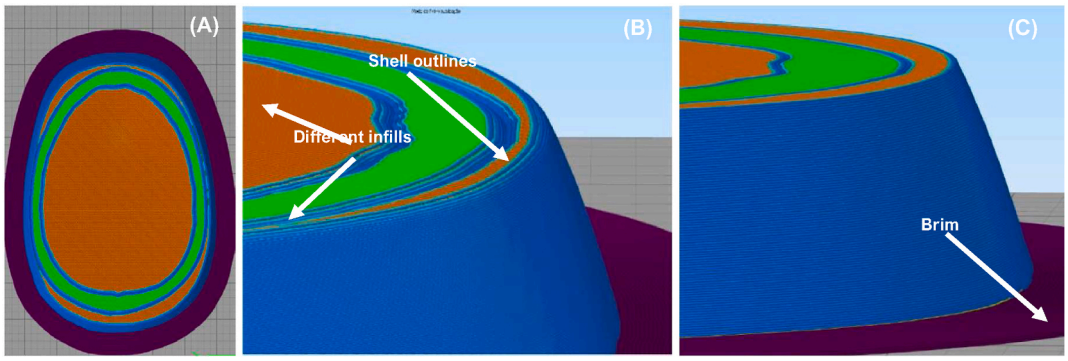

Fig. 7. Simplify3D software print planning. (A) overview of the slab to be printed. (B) Detail on shells outlines and different infill (C) Detail on the brim structure.

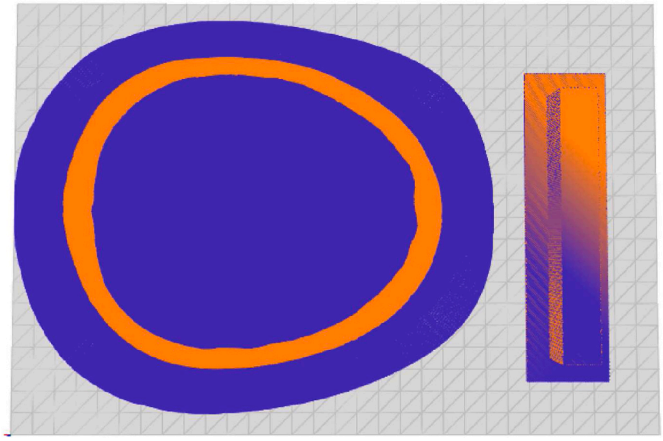

Fig. 8. Multi-material planning using 'Chroma' software.

Initially, three segmentations were created, representing bone tissue, soft tissue and air. Some minor adjustments were performed manually, specially to correct thin detailed anatomies, such as vertebral and temporomandibular joints, teeth insertions and soft nasal tissues. Also, whenever two distinct high attenuated structures were in contact, it would appear fused in the initial segmentation based on HU values, requiring manual separation.

Maxillary and mandibular teeth separation along the occlusal plane was performed, as well as the individual separation of each teeth's enamel, dentin, pulp and surrounding bone tissue. After the segmentation was completed, the main shape and tissue disposition was ready and mimicking the CIRS 711 phantom format (Fig. 4). Due to printing limitations of Simplify 3D software and the 3D printer used, it was not possible to print the phantom in a single piece. This led to split the head and neck segmentations in 58 segments distributed in 14 slabs of 20 mm thick (Fig. 4 E).

2.4. Setting up VID parameters and filament types

To use VID technique, a target HU to represent the human tissues were set at 75HU to soft tissue, and 450HU to in bone as these are typical numbers for these structures. Initially the plan was to use XCT – A for printing soft tissue (see details on the 3D printing material development at Savi et al., 2022). However, in the first VID planning it was realized that XCT-A was unable to perform the desired HU due to low infill limitation (at least 55% to not create grid appearance on CT). To solve this problem, the XCT manufacturer was asked to create and XCT filament with half attenuation of XCT-A. This new filament was named XCT-0 and had only 5% of radiopaque filler.

A new VID planning was performed, but in a first run of printing, it did not matter which printing configuration changed the results kept generating HU values over 50HU, below target. The solution for this came only after excluding material, CT scanner and planning possible problems. It was realized that yes, VID technique works, as the finger phantom printed in our previous work (Savi et al., 2020) achieved exactly what was planned, however, this actual attempt to produce a bigger phantom added a new variable, the size of it. All previous VID

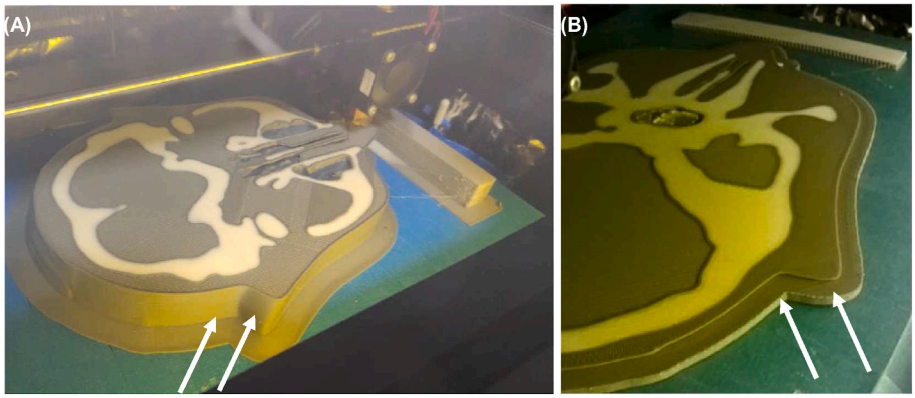

Fig. 9. Phantom print. (A) Beginning of brim contraction (white arrows) (B) detachment of the piece from the printing table.

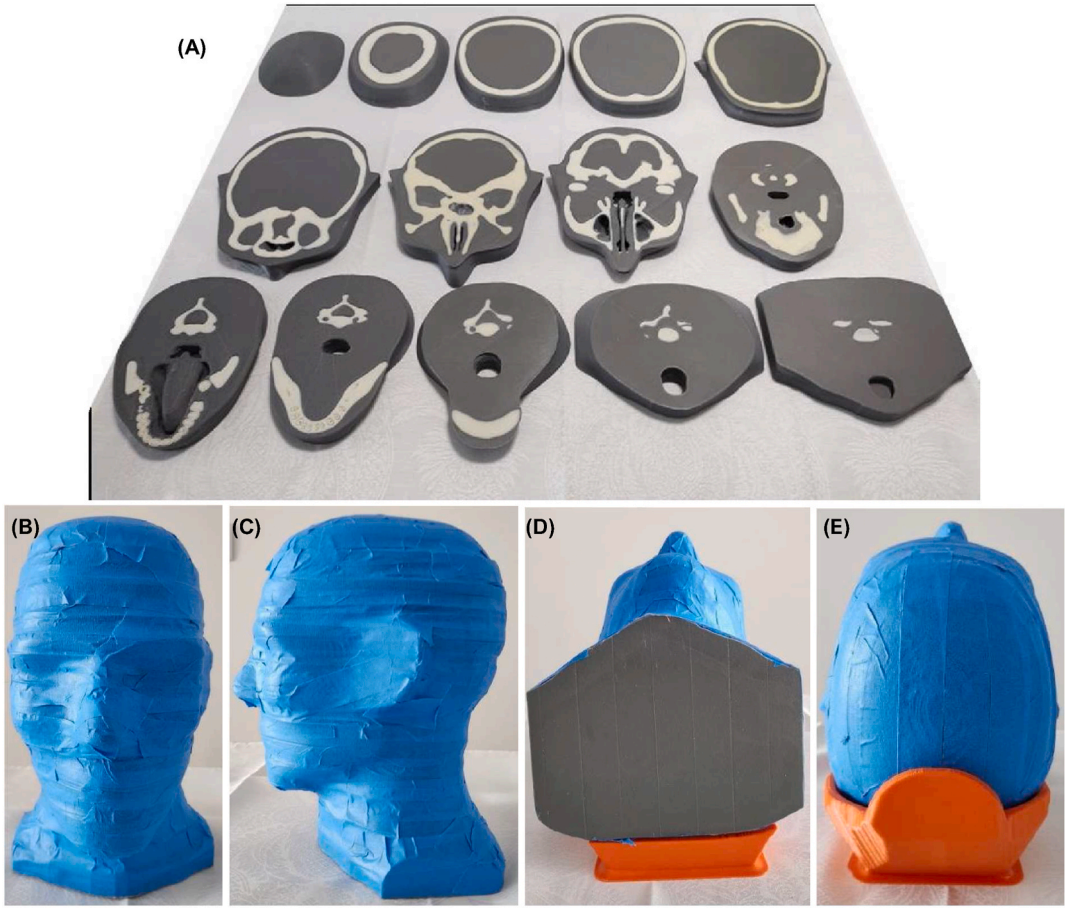

Fig. 10. (A) Overview of the slabs of the phantom printed (B) Assembled *"Blue Phantom"*, front view (C) Assembled *"Blue Phantom"*, lateral view (D) Assembled *"Blue Phantom"*, bottom view (E) Assembled *"Blue Phantom"*, top view.

calculations considered a 2 cm arrest cube that was used for verification of the finger with approximately 2 cm in diameter.

A new run of printing was carried out using 4 XCT filaments for printing cylinders with different diameters (2 cm, 4 cm, 8 cm, 12 cm) and different infills (40%, 60% and 80%) in order to investigate the variation of HU in the center of each cylinder. Fig. 5 shows the CT scout image of the printed test cylinders.

With this image acquisition, the HU numbers were evaluated. The cylinders were analyzed with a central ROI with a diameter so as to leave a minimum of 0.5 cm–1 cm from the edge. A linear ROI was also used for evaluation using the '*Image J*' software (Schneider et al., 2012) along its diameter. The information in Hounsfield units, pixel by pixel, is presented in Fig. 6.

Two facts are worth to be highlighted from these results: the first is that it is clearly demonstrated that the larger the diameter, the smaller the resulting Hounsfield number; second is that in all printed XCT filaments there is an exacerbation in the HU value at the edges, which indicates the hypothesis that the high atomic number of $BaSO_4$ inside the filaments promotes beam hardening.

The results confirm that as bigger the model is, less HU was measured in the center for the same infill percentage configuration. Therefore, the filaments chosen to be used to 3D print the phantom were as follows.

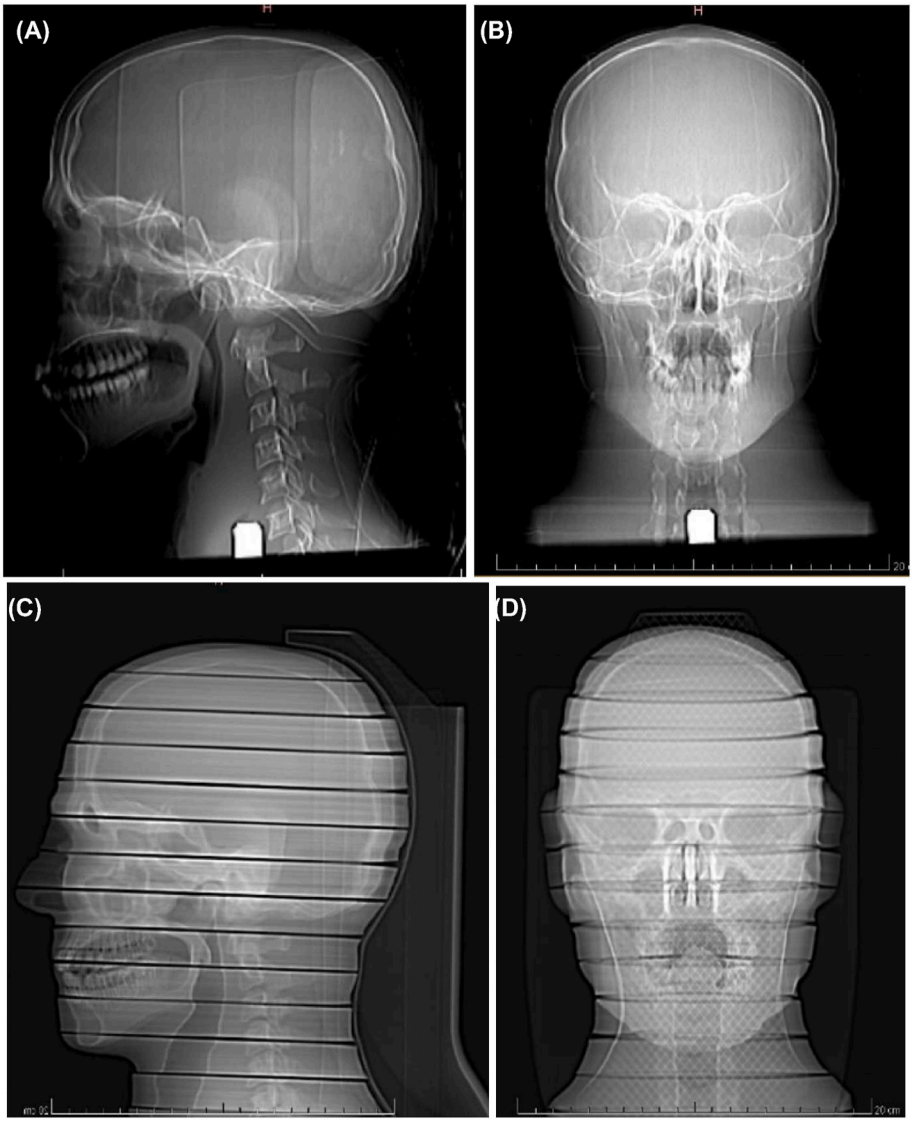

Fig. 11. Scout images of CIRS 711 phantom (A and B) and Scout images of the Blue Phantom (C and D).

- XCT – 0 for soft tissue,
- XCT – A to bone structures, and
- XCT – C to enamel and dentin.

More details on the characterization and development of these printing filaments can be found in Savi et al. (2021, 2022). With the estimation of the HU values, a "map" of printing configurations was created, and it was possible to determine the filling percentage value due to the diameter of the model, and due to the size of the piece. The results are presented in Table 1.

2.5. Setting up printing configurations

Some definitions of printing parameters should be highlighted. The first is that the chosen layer height was 0.2 mm and all models were made with two perimeter layers (shell). Despite some previous attempts showing the possibility of printing without a perimeter, when the piece was printed in direct contact with the table, there was a loss of adhesion, and the impression of the slice was unfeasible.

Also considering the lack of adhesion by contraction of ABS plastic, a structure called brim was added in the first three layers of printing. Several contours are added to the structure, in this case no less than 20 in order to try to minimize warping effects on each piece of the phantom printed (See Fig. 7).

Finally, after determining the printing parameters and subsequent export of the 3D model by Simplify3D, the model was then transferred to 'Chroma' software so that the multi material printing function could be added and the file rewritten to accommodate the color change that occurs in the transition tower, as seen in Fig. 8.

2.6. Printing the phantom

After investigations, the maximum air temperature that could be reached in the position where the thermocouples where was 70 ± 2 °C. Above this value, there was overheating of the heat sink located above the print nozzle. The exacerbated heating caused the filament to melt before reaching the nozzle, clogging of the nozzle and loss of printing.

The method to maintain a higher internal temperature inside the printer (described in section 2.2) to avoid warping of the printed piece was partially effective. In Fig. 9 one can verify this type of contraction and the detachment of the tip of the model from the table. This warp causes the extrusion nozzle to become compressed resulting in an increase in filling in this region due to material leakage and an under-extrusion that ends up discalibrating the material control of the

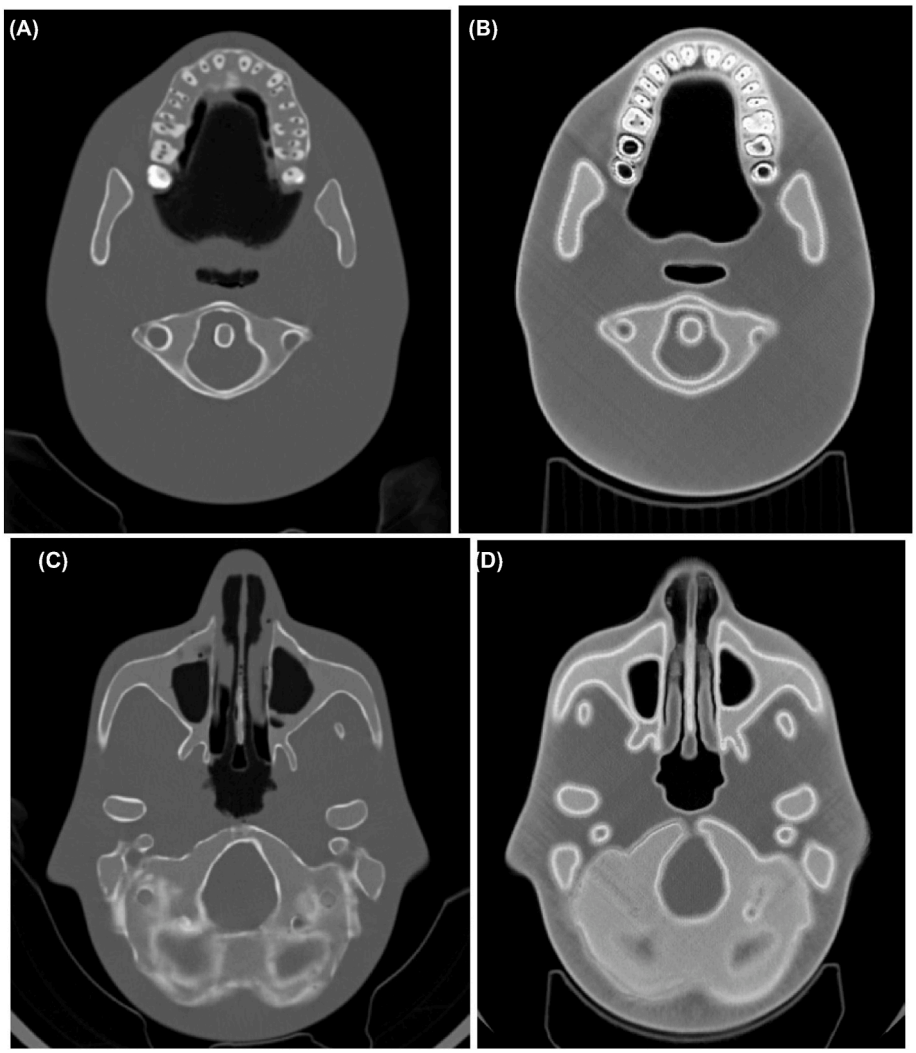

Fig. 12. Visual comparison between phantoms. Images on the right (A and C) are from CIRS 711 Atom Max phantom and images on the left (B and D) are from the 3D printed "Blue Phantom".

Mosaic Palette 2S. Contraction occurs, however, only at the edges of each piece, as one can see in Fig. 9B.

After printing, all the slabs were assembled using the same blue tape used for adhesion on the printing table. The tape was used only in the outside surface of the phantom, not in between each slab. After this procedure the phantom was named "*Blue phantom*" (Fig. 10).

3. CT imaging comparison between phantoms

3.1. Scout

Before each tomography, an exposure to X-rays is carried out to promote the planning of the exam to be performed, called "scout". Fig. 11 A to D shows the scout images of the CIRS 711 phantom and the Blue Phantom in anteroposterior (AP) and lateral (LAT) views. For comparison reasons, the same set up of windowing parameters of the images were used.

In Fig. 11 A and B, one can visualize the skull support used to perform the scan, as well as a radiopaque insert that corresponds to a thread where a tripod was attached. Fig. 11 C and D show incidences of the "*Blue Phantom*" and one can observe by comparing these images that the mounting of the slabs of the "*Blue Phantom*" is very visible. The "*Blue Phantom*" is more homogeneous than the CIRS 711 in terms of gray tones and with some more evident anatomical landmarks, such as the region of the mouth, larynx, pharynx, as well as the cortical bones.

3.2. Slice-by-slice visual comparison

A slice-by-slice visual comparison was made, and we have chosen to document in this paper a slice with anatomical complexity and different materials representation, as one can see in Fig. 12. Small anatomical variations between the teeth and their surroundings can be seen since these regions were segmented practically manually and modified with the intention of making these structures more realistic (Fig. 12 A and B).

In Fig. 12 C and D, there were visual regions with a greater number of HU, especially in the initial centimeters in relation to the edges of the image. This phenomenon is probably due to the high attenuation of the XCT-A filament used as bone and this specific reconstruction algorithm.

3.3. Hounsfield numbers evaluation

Fig. 13 and Table 2 present the HU numbers evaluation through circular ROI. Using the described method and considering the problem of decreasing the HU towards the center of the piece, the result referring to this part of the study was partially achieved. In Fig. 13 A and B shows that the goal of reaching values close to 75 HU was achieved. However, in the upper slices of the phantom, such as number 3, shown in Fig. 13 C, the HU obtained was different from what had been planned. This was

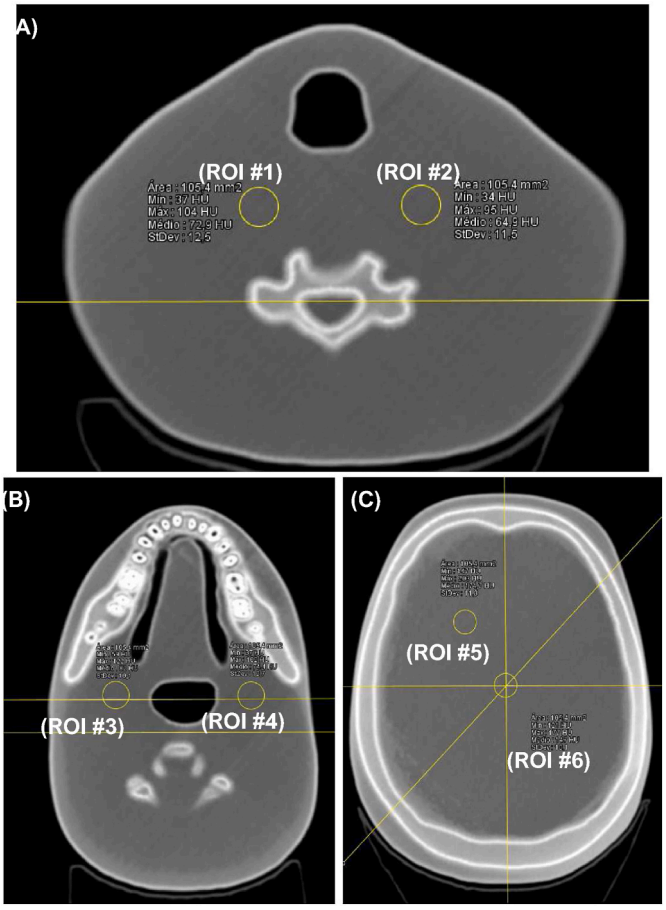

Fig. 13. Measurement of the Hounsfield number in some layers of the phantom. (A) Slab 13, (B) Slab 10 and (C) Slab 5.

Table 2
HU evaluation of the *"Blue Phantom"*.

	Fig. 13 A		Fig. 13 B		Fig. 13 C	
	ROI #1	ROI #2	ROI #3	ROI #4	ROI #5	ROI #6
Min	37	34	59	37	147	121
Max	104	95	122	102	203	177
Mean	72.9	64.9	82	74.4	174.7	147
SD	12.5	11.5	10.1	12.7	11.3	10.1

due to the lack of checking these layers after printing, as was done with the previous ones. Two factors contributed to this happening: the lack of time for printing and the temporary unavailability of the CT scanner used for the analyses.

In order to delve deeper into the analysis of the HU numbers of the "*Blue Phantom*" slices, Fig. 14 presents the graphic plots of the linear ROIs represented in Fig. 13 in the form of yellow lines. In the graphs, it is possible to verify the variations during the analysis, pixel by pixel. Assuming close to the desired value in slices 13 and 10, the variation can be considered significant, since the desirable thing was for the value to be around that selected in the calculations.

In all graphic plots, an almost exponential curve of HU values is identified from the edge towards the center of the model, more evident in slices 13 and 10. Another noticeable point with this analysis technique is that this increase in values tends to happen more sharply on the right side of the graphics, which corroborates the printing defects, mainly with the greater contraction of the material on one side of the printing. In addition to material contraction, as previously discussed, other reasons that may be related to this increase in HU are the amount

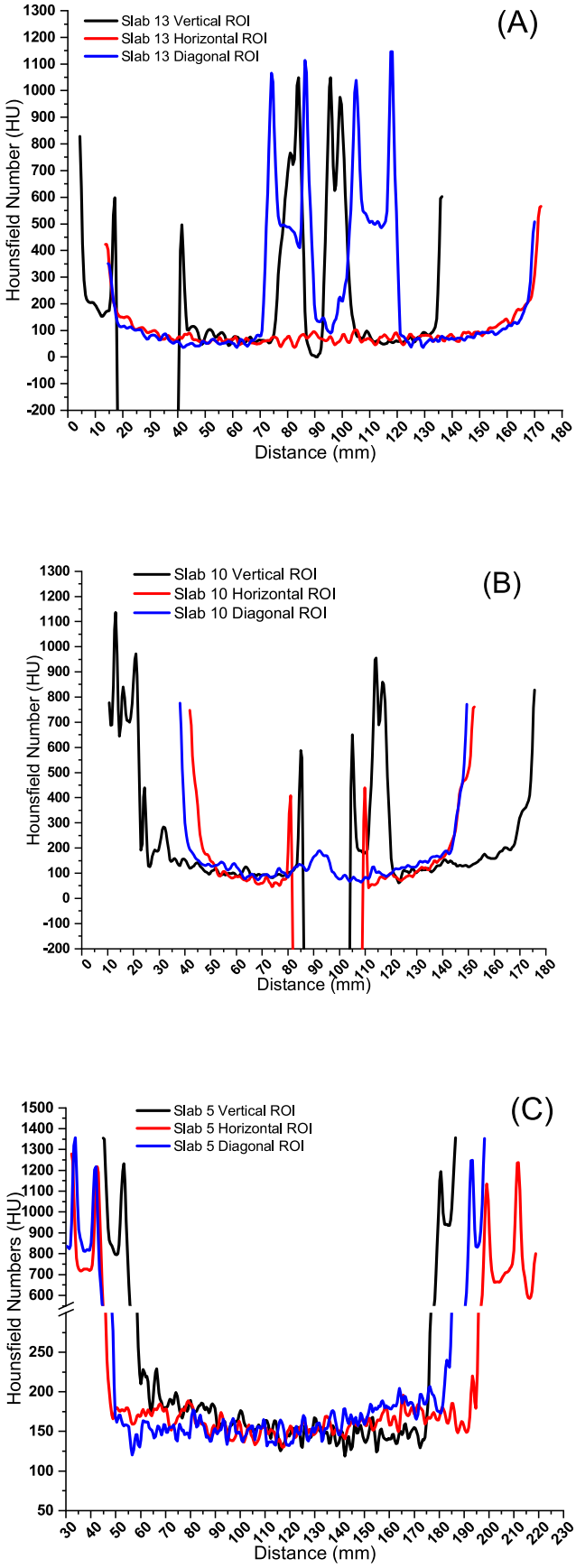

Fig. 14. Graphic plots of the linear ROI's. (A) Slab 13, (B) Slab 10 and (C) Slab 5.

of barium sulfate used as an attenuator, as well as the reconstruction algorithms.

4. Achievements and outlook

This work opens a range of possibilities to be studied in the future. For example, and which is already being done within our group research, the creation of PLA-based XCT filaments to avoid deformations due to material contraction. In addition to the existing XCT profiles (0, A, B and C), an XCT based on calcium carbonate instead of barium sulfate is also under development. Due to the fact that it has much lower attenuation than barium, the filling variation has the possibility of creating a fine adjustment of HU in the soft tissue representations.

Visually, two items were observed on the HU evaluation tomographic image. The first is the appearance of lines in models with a filling percentage lower than 50–55%, depending on the material, so that to remedy this problem a simple infill adjustment was enough. The use of 'shells' in the printed models generated radiopaque edges in the tomographic image. The evaluations carried out showed that this factor is related not only to their use or not, but also to the mathematical reconstruction algorithms of the tomographic image.

As recommended by the publication 44 of ICRU (ICRU, 1989), to validate the tissue equivalence of these materials, parameters like the chemical composition, mass attenuation coefficient, mass stopping power, bulk density, electronic density, depth dose profile and Hounsfield units should be evaluated. The validation of PLA as a soft tissue simulator for 3D printed phantoms for radiotherapy applications was described in previous works (Pereira et al., 2021, 2022). In this paper we aimed to describe the CT imaging behavior of the 3D printed *"Blue Phantom"* in terms of Hounsfield units in comparison with the CIRS 711 Atom Max phantom and the methodology to achieve this. More investigations are required to guarantee if this method also provides tissue equivalence to the phantom in accordance with ICRU 44 standards.

It is also possible to replace the printed soft tissue with resins based on acrylic, epoxy, polyurethane, among others, not to mention the use of silicone or polyurethane rubber. This method would reduce printing time of the phantom but additional care regarding impermeabilization may be required (Villani, 2021). The gaps between the slabs and its imaging artifacts are part of the intrinsic characteristics of using these 3D printing technique and materials. A possible solution to reduce this effect is to slip the phantom in fewer number of slabs.

There is still the need to improve the teeth printing configuration, aiming to use other 3D programming methods to make them more reliable. In this way, studies must be performed on the use of the CURA software in order to eliminate the excess of internal perimeters, e. g. fine tuning of the extrusion rate of the printing materials, enabling the printing of the phantom in a single run.

CRediT authorship contribution statement

M. Savi: Writing – review & editing, Validation, Methodology, Investigation, Formal analysis, Data curation, Conceptualization. **D. Villani:** Writing – review & editing, Writing – original draft, Validation, Methodology, Investigation, Formal analysis, Data curation. **B. Andrade:** Visualization, Validation, Project administration, Investigation, Formal analysis, Data curation, Conceptualization. **F.A.P. Soares:** Visualization, Validation, Methodology, Investigation, Formal analysis. **O. Rodrigues Jr.:** Supervision, Resources, Project administration, Funding acquisition. **L.L. Campos:** Writing – review & editing, Supervision, Resources, Funding acquisition. **M.P.A. Potiens:** Supervision, Project administration, Funding acquisition.

Declaration of competing interest

The authors declare the following financial interests/personal relationships which may be considered as potential competing interests: Leticia Lucente Campos reports financial support was provided by State of Sao Paulo Research Foundation. Daniel Villani reports financial support was provided by National Council for Scientific and Technological Development. If there are other authors, they declare that they have no known competing financial interests or personal relationships that could have appeared to influence the work reported in this paper.

Data availability

Data will be made available on request.

Acknowledgments

The authors would like to thank São Paulo Research Foundation – FAPESP (process numbers 2017/50332-0 and 2018/05982-0) and National Council for Scientific and Technological Development - CNPq (process numbers 312131/2016-0 and 142098/2017-5) for the financial support.

References

Abdel Magid, B.M., Vanoosten, D., Vrieze, T., Leng, S., 2018. Composite materials for 3D printing of medical phantoms. In: CAMX 2018 - Composites and Advanced Materials Expo, 8928008.

AII3DP, 2023. PolyJet 3D printing – the ultimate guide. What Is PolyJet 3D Printing? Available at: https://all3dp.com/2/polyjet-3d-printing-technologies-simply-explained/.

Andrade, M.A.B., Savi, M., Alves, C.O., Fin, A.P.C., Soares, F.A.P., Potiens, M.P.A., 2020. Impact of infill percentages in visual homogeneity for 3D printed imaging phantoms. Brazilian Journal of Radiation Sciences.

Andrade, Marco Antônio, Bertoncini, Ana Paula Chaise, Fin, Caroline de Oliveira, Alves, Flávio Augusto Penna, Soares, Savi, Bianchi, Matheus Brum Marques, Maria da Penha Albuquerque Potiens, 2020. Visual impact of infill percentages for 3D printed radiologic simulators. Brazilian Journal of Radiation Sciences 8 (1A). Suppl.

Bandyopadhyay, Amit, Vahabzadeh, Sahar, Shivaram, Anish, Bose, Susmita, 2015. Three-dimensional printing of biomaterials and soft materials. MRS Bull. 40 (12), 1162–1169. https://doi.org/10.1557/mrs.2015.274.

Craft, D.F., Howell, R.M., Fox, C.J., Surry, D., Kry, S.F., 2018. 3D printing and its use in radiation therapy dosimetry. Australas. Phys. Eng. Sci. Med. 41 (1), 1–14. https://doi.org/10.1007/s13246-017-0602-0.

DeWerd, L.A., 2014. In: Kissick, Michael (Ed.), The Phantoms of Medical and Health Physics. Springer, Berlin.

Diamantopoulos, S., et al., 2018. Theoretical and experimental determination of scaling factors in electron dosimetry for 3D-printed polylactic acid. Medical physics 45 (4), 1708–1714.

Filippou, V., Tsoumpas, C., 2018. Recent advances on the development of phantoms using 3D printing for imaging with CT, MRI, PET, SPECT, and ultrasound. Medical physics 45 (9), e740–e760.

Gibson, Ian, Rosen, David, Stucker, Brent (Eds.), 2015. Additive Manufacturing Technologies: 3D Printing, Rapid Prototyping, and Direct Digital Manufacturing, vol. 2. Springer, New York, NY. Online-Ressource (XXI, 498. (SpringerLink : Bücher). ISBN 978-1-4939-2113-3.

Hamedani, B.A., et al., 2018. Three-dimensional printing CT-derived objects with controllable radiopacity. J. Appl. Clin. Med. Phys. 19 (2), 317–328.

Hong, Dayeong, et al., 2020. Development of a CT imaging phantom of anthromorphic lung using fused deposition modeling 3D printing. Medicine 99, 1.

ICRU, 1989. Report 44. Tissue substitutes in radiation dosimetry and measurement. J. Int. Comm. Radiat. Units Meas. 23 (1), 1–189.

Niebuhr, N.I., et al., 2019. The ADAM-pelvis phantom—an anthropomorphic, deformable and multimodal phantom for MRgRT. Phys. Med. Biol. 64 (4), 04NT05.

Okkalidis, N., Chatzigeorgiou, C., Okkalides, D., 2018. Assessment of 11 available materials with custom three-dimensional-printing patterns for the simulation of muscle, fat, and lung Hounsfield units in patient-specific phantoms. Journal of Engineering and Science in Medical Diagnostics and Therapy 1 (1), 1–7.

Oliveira, Marcus, Savi, Matheus, Andrade, Marco, Villani, Daniel, Potiens, Maria da Penha Albuquerque, Stuani, Hector, Ubeda, Carlos, Mdletshe, Sibusiso, 2022. Attenuation properties of common 3D printed FFF plastics for mammographic applications. Brazilian Journal of Radiation Sciences 10 (1).

Pereira, D.D., Cardoso, S.C., da Rosa, L.A.R., de Souza, F.M.L., de Sousa, J.V.M., Batista, D.V.S., et al., 2021. Validation of polylactic acid polymer as soft tissue substitutive in radiotherapy. Radiat. Phys. Chem. 189, 109726 https://doi.org/10.1016/j.radphyschem.

Pereira, Dirceu D., Cardoso, Simone C., Batista, Delano VS., de Souza, Felipe ML., de Sousa, Juan VM., Gonçalves, Odair D., da Rosa, Luiz AR., 2022. Development of an anthropomorphic phantom based on 3D printing for assessment of dose delivered to the eye and adjacent tissues. Radiat. Phys. Chem. 199, 110292 https://doi.org/10.1016/j.radphyschem.2022.110292.

Ramian, J., Ramian, J., Dziob, D., 2021. Thermal deformations of thermoplast during 3D printing: warping in the case of ABS. Materials 14 (22), 7070.

Rengier, F., et al., 2010. 3D printing based on imaging data: review of medical applications. Int. J. Comput. Assist. Radiol. Surg. 5, 335–341. https://doi.org/10.1007/s11548-010-0476-x.

Santos, J.C., et al., 2019. Characterization and applicability of low-density materials for making 3D physical anthropomorphic breast phantoms. Radiat. Phys. Chem., 108361

Shapira, Nadav, et al., 2022. PixelPrint: three-dimensional printing of realistic patient-specific lung phantoms for validation of computed tomography post-processing and inference algorithms. medRxiv 2022, 05.

Savi, Matheus, Andrade, Marco AB., Potiens, Maria PA., 2020. Commercial filament testing for use in 3D printed phantoms. Radiat. Phys. Chem. 174, 108906.

Savi, M., Villani, D., Andrade, M.A.B., Rodrigues Jr., O., Potiens, M.P.A., 2021. Study on attenuation of 3D printing commercial filaments on standard x-ray beams for dosimetry and tissue equivalence. Radiat. Phys. Chem. 182, 109365.

Savi, M., Andrade, M.A.B., Villani, D., Rodrigues Jr, O., Potiens, M.P.A., 2022. Development of radiopaque FFF filaments for bone and teeth representation in 3D printed radiological objects. Brazilian Journal of Radiation Sciences 10 (1).

Schneider, C.A., Rasband, W.S., Eliceiri, K. W. Nih, 2012. Image to Image J: 25 years of image analysis. Nat. Methods 9 (7), 671–675.

Tino, Rance, et al., 2021. The interlace deposition method of bone equivalent material extrusion 3D printing for imaging in radiotherapy. Mater. Des. 199, 109439.

Tong, Huayu, et al., 2019. Controlling the position-dependent contrast of 3D printed physical phantoms with a single material. In: Medical Imaging 2019: Physics of Medical Imaging, vol 10948. SPIE.

Villani, D., Rodrigues Jr., O., Campos, L.L., 2020. Dosimetric characterization of 3D printed phantoms at different infill percentages for diagnostic X-ray energy range. Radiat. Phys. Chem. 172, 108728.

Villani, D., 2021. Desenvolvimento de um simulador antropomórfico de pescoço-tireoide tecido-equivalente impresso em 3D para aplicações multidisciplinares. Universidade de São Paulo. PhD diss.